

TWO DIMENSIONAL TOPOLOGY OF COSMOLOGICAL REIONIZATION

YOUANG WANG¹, CHANGBOM PARK², YIDONG XU¹, XUELEI CHEN^{1,3}, JUHAN KIM⁴

Draft version March 6, 2022

ABSTRACT

We study the two-dimensional topology of the 21-cm differential brightness temperature for two hydrodynamic radiative transfer simulations and two semi-numerical models. In each model, we calculate the two dimensional genus curve for the early, middle and late epochs of reionization. It is found that the genus curve depends strongly on the ionized fraction of hydrogen in each model. The genus curves are significantly different for different reionization scenarios even when the ionized fraction is the same. We find that the two-dimensional topology analysis method is a useful tool to constrain the reionization models. Our method can be applied to the future observations such as those of the Square Kilometer Array.

Subject headings: dark matter – galaxies:halos – galaxies:structure – large-scale structure of universe – methods : statistical

1. INTRODUCTION

Reionization is a milestone event in the history of the universe. Quasar absorption line observations indicate that its completion is at redshift $z \gtrsim 6.5$ (e.g. Fan et al. 2006). The history of the epoch of reionization (EoR) remains unclear, but the cosmic microwave background (CMB) signal show that the total optical depth of free electrons is $\tau = 0.066 \pm 0.016$, corresponding to $z_{re} = 8.8^{+1.7}_{-1.4}$ if the reionization happens suddenly at a redshift z_{re} (Planck Collaboration et al. 2015), so its beginning must be earlier. The complex reionization process has been investigated by many theoretical works (e.g. Furlanetto et al. 2004; Choudhury & Ferrara 2007; Zhang et al. 2007; Xu et al. 2009; Yue et al. 2009; Yue & Chen 2012; Kim et al. 2013). One of the most promising methods to detect the cosmic reionization is through the 21 cm transition of HI. The emission or absorption of the 21 cm line traces the neutral hydrogen well at different redshifts, which can provide us with the most direct view of the reionization history.

Due to the strong foregrounds, the observation of high redshift 21 cm signals is a challenging task. Although there are a number of running radio interferometer arrays, such as the 21 Centimeter Array (21CMA; Wu 2009); the Giant Metre-wave Radio Telescope (GMRT; Paciga et al. 2013), which gives a constraint on reionization at $z \approx 8.6$; the Low Frequency Array (LOFAR; Rottgering et al. 2006), the Murchison Widefield Array (MWA; Bowman et al. 2013; Tingay et al. 2013); and the Precision Array for Probing the Epoch of Reionization (PAPER; Jacobs et al. 2015), which is designed for observing the redshift 21cm signal from EOR and gives a new 2σ upper limit on $\Delta^2(k)$ of $(22.4\text{mK})^2$ in the range

$0.15 < k < 0.5 h\text{Mpc}^{-1}$ at $z = 8.4$.

Additionally, the kinematic Sunyaev-Zel'dovich (kSZ; Sunyaev & Zeldovich 1972, 1980) can distort the primary CMB black-body spectrum due to the peculiar velocity of the clusters of galaxies. During the reionization, the ionized bubbles generate angular anisotropy through the kSZ effect. The amplitude of kSZ power depends on the process of reionization, and its shape depends on the distribution of bubble size. Therefore, the kSZ power spectrum can give constraints on the epoch of reionization (Mortonson & Hu 2010; Zahn et al. 2012; Mesinger et al. 2012; George et al. 2015). When the post-reionization homogeneous kSZ signal is taken into account, George et al. (2015) found an upper limit on the duration $\Delta z < 5.4$ at 95% CL.

At present, the reionization process is studied by numerical simulations (e.g. Iliev et al. 2006; Trac & Cen 2007; Trac et al. 2008; Cen et al. 2009; Yue & Chen 2012; Battaglia et al. 2013; Iliev et al. 2014) or semi-numerical simulations (e.g. Mesinger & Furlanetto 2007; Mesinger et al. 2011; Majumdar et al. 2014), and different reionization scenarios can be explored by varying the input parameters of the models. We expect the 21cm signal from the EoR to be detected in the near future, and the data will help constrain the theoretical models.

One popular way of analyzing 21 cm observation is to use the power spectrum of the neutral hydrogen (Lewis & Challinor 2007; Liu & Tegmark 2011; Mao et al. 2012; Mao 2014). Recently, an alternative approach based on the topological analysis has been used to quantify the ionization status of the intergalactic medium (Lee et al. 2008; Hong et al. 2014). The topological analysis was introduced to cosmology as a method to test the Gaussianity of the primordial density field as predicted by many inflationary scenarios (Gott et al. 1986), and this tool has been developed and applied during the past 20 years (Hamilton et al. 1986; Gott et al. 1987, 1989, 2008, 2009; Park & Gott 1991; Park et al. 1992, 2005b,a; Vogeley et al. 1994). The genus of isodensity surfaces has been used to quantify the spatial distribution of galaxies and to constrain the galaxy formation models (Park et al. 2005b; Choi et al. 2010). Compared with the power spectrum, the topology method has certain niches.

¹ Key Laboratory of Computational Astrophysics, National Astronomical Observatories, Chinese Academy of Sciences, Beijing, 100012 China; E-mail: wangyg@bao.ac.cn

² School of Physics, Korea Institute for Advanced Study, 85 Hoegiro, Dongdaemun-gu, Seoul 130-722, Korea; cbp@kias.re.kr

³ Center for High Energy Physics, Peking University, Beijing 100871, China

⁴ Center for Advanced Computation, Korea Institute for Advanced Study, 85 Hoegiro, Dongdaemun-gu, Seoul 130-722, Korea

The topology of the isodensity contours is insensitive or less sensitive to nonlinear gravitational evolution, galaxy bias and the redshift distortion, since the the intrinsic topology does not change as the structures grow, at least not until the eventual break at shell crossing (Park et al. 2005a; Park & Kim 2010; Wang et al. 2012).

In this paper, we use the 2d genus to characterize the different reionization models. Compared with the 3d genus, the 2d genus method can be applied to two-dimensional or nearly two-dimensional data sets, such as the cosmic microwave background. Although the three-dimensional data cube can be obtained in HI observations, in some cases the foreground removal process limit us to use the two-dimensional data. Secondly, it saves much time to compute the 2d genus than that the 3d one. One of the processes (convolved by the smoothing filter) of the genus calculation is the Fast Fourier Transform (FFT). The speed of FFT is proportional to $N \log N$, where N is the total of number of data points, which is related to the data points (N_c) in each dimension as $N = N_c^2$ and $N = N_c^3$ in two and three dimensions, respectively. Therefore, the time taken in 3d genus is at least of $1.5N_c$ times in 2d genus. Even if the 3d genus can be obtained, the 2d genus can provide a useful cross check.

Below, we introduce the calculation of the 21 cm differential brightness temperature and its 2d genus curve in Sec.2. In Sec. 3 we describe the radiative transfer simulations and semi-numerical simulation used in this paper. Our results are presented Sec.4. We summarize and discuss the results in Sec. 5.

2. THE TWO-DIMENSIONAL GENUS OF 21CM TEMPERATURE

2.1. The 21 cm signal

The emission or the absorption of 21 cm signal depends on the spin temperature T_S of neutral hydrogen, which is defined by the relative number densities, n_i , of atoms in the two hyperfine levels of the electronic ground state, $n_1/n_0 = 3 \exp(-T_\star/T_S)$, where $T_\star = h_p \nu_{10}/k_B = 0.068 K$ is the equivalent temperature of the energy level hyperfine structure splitting $h_p \nu_{10} = 5.9 \times 10^{-6} \text{eV}$. The spin temperature T_S is determined by several competing processes (c.f. Furlanetto et al. (2006)):

$$T_S^{-1} = \frac{T_\gamma^{-1} + x_c T_K^{-1} + x_\alpha T_C^{-1}}{1 + x_c + x_\alpha} \quad (1)$$

where $T_\gamma = 2.726(1+z)K$ is the cosmic microwave background (CMB) temperature at redshift z , T_K is the gas kinetic temperature, T_C is the effective color temperature of the UV radiation, x_c is the coupling coefficient for collisions and x_α is the coupling coefficient for UV scattering. Comparing with the CMB temperature, the 21 cm radiation is observed in emission if $T_S > T_\gamma$, or absorption if $T_S < T_\gamma$. Generally, the 21 cm signal is quantified by the 21 cm differential brightness temperature,

$$\delta T_b = \frac{T_S - T_\gamma}{1 + z} (1 - e^{-\tau}), \quad (2)$$

where the optical depth τ is produced by a patch of neutral hydrogen, which has the following form

(Furlanetto et al. 2006; Barkana & Loeb 2001)

$$\tau(z) = (2.8 \times 10^{-4}) \left(\frac{T_S}{1000 \text{ K}} \right)^{-1} \left(\frac{h}{0.70} \right) \left(\frac{1+z}{10} \right)^{3/2} \times \left(\frac{\Omega_b}{0.046} \right) \left(\frac{\Omega_m}{0.28} \right)^{-1/2} (1 + \delta). \quad (3)$$

Here δ is the density contrast. Assuming $\tau \ll 1$ and $T_s \gg T_\gamma$, then the brightness temperature of the 21cm emission can be written as

$$\delta T_b = (28 \text{ mK}) \left(\frac{h}{0.72} \right) \left(\frac{1+z}{10} \right)^{1/2} \left(\frac{H}{dv_r/dr + H} \right) \times \left(\frac{\Omega_b}{0.044} \right) \left(\frac{\Omega_m}{0.26} \right)^{-1/2} (1 + \delta)(1 - x_i). \quad (4)$$

where x_i is the fraction of ionized hydrogen, $H(z)$ is the Hubble parameter, dv_r/dr is the comoving gradient of the line-of-sight (LOS) component of the comoving velocity. It is noted that the distribution of the brightness temperature of the neutral hydrogen will be the same as that of the underlying matter density field if dv_r/dr is small ($dv_r/dr \ll H$) and the gas is fully neutral ($x_i = 0$).

2.2. The 2d genus

The 2d genus has been applied in many fields, such as the cosmic microwave background fluctuations (Colley et al. 1996; Park et al. 1998), weak lensing field Matsubara & Jain (2001); Sato et al. (2003), non-Gaussian signatures (Park 2004), large-scale structure in the redshift survey (James et al. 2007), galaxy distribution in the Hubble deep fields (Park et al. 2001), neutral hydrogen in both the Large and Small Magellanic Cloud (Kim & Park 2007; Chepurnov et al. 2008).

If we consider the 21cm brightness temperature on a spherical shell, the 2d genus of the contour is defined by the number of contours surrounding regions higher than a threshold value minus the number of contours enclosing regions lower than the threshold (Melott et al. 1989; Gott et al. 1990; Park et al. 2013)

$$G(\nu) = N_{\text{high}} - N_{\text{low}} \quad (5)$$

where N_{high} and N_{low} are the number of isolated high-density regions and low-density regions, respectively. The genus $G(\nu)$ depends on the threshold density value ν , which is in units of standard deviation from the mean. Given a two-dimensional distribution, the 2d genus can be measured by using the Gauss-Bonnet theorem (Gott et al. 1990)

$$G_{2d} = \frac{\int C dS}{2\pi} \quad (6)$$

where the integral line is along the contour, and C is the inverse curvature r^{-1} of the line. The value of 2d genus maybe negative or positive, depending on whether a low- or high-density region is enclosed. If a curvature is integrated along a closed contour around a high-density region, its value will be 1, otherwise, its value is -1. For a Gaussian random field, the 2d genus per unit area is

given by (Melott et al. 1989; Coles 1988)

$$G_{2d,Gaussian} = \frac{1}{(2\pi)^{3/2}} \frac{\langle k^2 \rangle}{2} \nu \exp(-\nu^2/2) \quad (7)$$

where $\langle k^2 \rangle = \int k^2 P_2(k) d^2k / \int P_2(k) d^2k$ is the square of the wavenumber k averaged over the smoothed two-dimensional power spectrum $P_2(k)$. In practice, the one-point distribution of the density field is not interesting (Vogeley et al. 1994; Park et al. 2001), we follow (Park et al. 2001) to parametrize the area fraction by

$$f_A = \frac{1}{\sqrt{2\pi}} \int_{\nu_A}^{\infty} e^{-t^2/2} dt \quad (8)$$

The genus is calculated from $\nu_A = -3$ to 3 within an interval of 0.2. Here we use the numerical code `contour2d` to calculate the 2d genus (Gott et al. 1986; Melott et al. 1989). In this code, the 2d genus is calculated by counting the turning of a contour observed at each vertex of four pixels: 1/4 contribution is from each vertex with 1 high density-region pixel and 3 low-density region pixels, -1/4 from each vertex with 3 high density-region pixel and 1 low-density region pixels, and otherwise is zero.

3. SIMULATIONS

Our reionization models are different from what was used in the work of Hong et al. (2014). They used the N-body simulation and $C^2 - \text{Ray}$ (Mellema et al. 2006) method. Here we use the hydrodynamic radiative transfer (HRT) simulations (Trac et al. 2008) and the semi-numerical model 21cmFAST Mesinger et al. (2011). The main advantage of the HRT simulation over the simulation in Hong et al. (2014) is that it is a real hydrodynamical simulation which keeps track of baryon evolution, heating, and cooling processes. The 21cmFAST routine is an approximation to the HRT simulation, and it is faster than both simulation in Hong et al. (2014) and the HRT simulation.

Throughout the paper, we use the Wilkinson Microwave Anisotropy Probe (WMAP) 5 year cosmological parameters: $\Omega_m = 0.258$, $\Omega_\Lambda = 0.742$, $\Omega_b = 0.044$, $h = 0.719$, $\sigma_8 = 0.796$, and $n_s = 0.963$ (Dunkley et al. 2009), which are consistent with the cosmology parameters in the HRT simulation used in this study.

3.1. cosmological radiative transfer simulation

The hydrodynamic radiative transfer simulations used in this paper was described in detail in Trac et al. (2008). The simulation is based on the numerical method described in Trac & Cen (2007), which includes an N -body algorithm for dark matter, a star formation prescription, and a radiative transfer algorithm for ionizing photons. The N -body simulation includes 3072^3 dark matter particles on an effective mesh with $11,520^3$ cells in a comoving box, $100h^{-1}\text{Mpc}$ on each side. The mass of each dark matter particle is $2.68 \times 10^6 M_\odot$. The resolution of hydrodynamic+RT simulations is $N = 1536^3$ of dark matter particles, gas cells, and adaptive rays. The photoionization and photoheating rates are calculated for each cell.

Star formation occurs for particles with the density $\rho_m > 100\rho_{\text{crit}}(z)$ and temperature $T > 10^4$ K. This cut in the temperature-density phase space restricts star for-

mation effectively to regions within the virial radius of halos that cool efficiently through atomic line transitions.

Here we use two groups of the HRT simulations, which have different finishing time for the hydrogen reionization. In the first simulation, the reionization is completed late at $z \sim 6$ (HRT sim1), while in the second simulation the reionization is finished early at $z \sim 9$ (HRT sim2).

3.2. The semi-numerical simulation 21cmFAST

We also use a semi-analytical code 21cmFAST (Mesinger et al. 2011) to study the cosmological 21 cm signal. The 21cmFAST code is a useful semi-numerical code to model the reionization process. Given the box size and particle number, the Gaussian random initial conditions of the dark matter density and velocity fields are generated by Monte Carlo sampling method. The large-scale density and peculiar velocity field are then obtained by first-order perturbation theory. Assuming that the number of ionizing photons are proportional to the collapse fraction computed from the extended Press-Schechter formalism, the ionization field is generated from the evolved density field at each redshift. From the density, ionization and peculiar velocity, the 21cm brightness temperature is obtained. The advantage of this approach is that it is very fast to calculate the 21 cm signal for different model parameters.

In order to match the completion time of the cosmic reionization in the HRT simulation, we change the ionizing efficiency factor ζ , which is defined as $\zeta = f_{\text{esc}} f_\star N_{\gamma/b} n_{\text{rec}}^{-1}$. Here f_{esc} is the escape fraction of ionizing photons from the object, f_\star is the star formation efficiency, $N_{\gamma/b}$ is the number of ionizing photons produced per baryon in stars, and n_{rec} is the typical recombined number of times for a hydrogen atom. The box size is the same as in HRT simulations, the cell number is $N = 768^3$. The cosmology parameters in our 21cmFAST simulation are chosen to be the same as in the HRT simulation, which is based on the WMAP5 data. We have run two simulations ($\zeta = 15$ for 21cmFAST1 and $\zeta = 50$ for 21cmFAST2) by using the 21cmFAST code. The finishing time of reionization is $z \sim 6$ in 21cmFAST1 and $z \sim 9$ in 21cmFAST2. Combined with two HRT simulations, we define HRT sim1 and 21cmFAST1 as the two *late models*, while HRT2 and 21cmFAST2 as the two *early models*.

It is interesting to compare the different models at a fixed ionization fraction. Therefore, we output one snapshot of 21cmFAST1 simulation which has the same ionization fraction as the one from HRT sim1 at $x_i = 0.65$, and another snapshot from 21cmFAST2 with the same ionization fraction from HRT sim2 at $x_i = 0.55$. The two thin vertical lines in Figure 1 show $x_i = 0.55$ and $x_i = 0.65$.

For the 21cmFAST simulation, we shall compare the 2d genus curve of the differential brightness temperature with that of the matter distribution. For the HRT simulations, the dark matter and gas components are separate, so we shall show the genus curve of gas for comparison.

In Figure 1, we show the evolution of ionization fraction of the neutral hydrogen fraction (low) and the relation between the ionization fraction and the average differential brightness temperature (up) of 21 cm signal in four simulations. The ionization fraction x_i increases

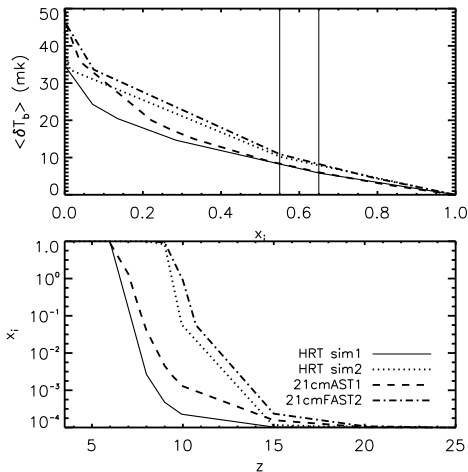


FIG. 1.— Lower Panel: Evolution of the ionization fraction as a function of redshift for the different models. Upper Panel: Relation between the ionization fraction and the average differential brightness temperature of 21cm signal. The two thin vertical lines indicate $x_i = 0.55$ and $x_i = 0.65$, respectively.

rapidly with the decreasing redshift, and the mean differential brightness temperature decreases rapidly with time. In other words, the full reionization processes are fast in these models. The HRT sim1 and the 21cmFAST1 have the same reionization completion time and the same ionization fraction at one redshift, but the ionization fractions at other redshifts are different. The simulations HRT sim2 and 21cmFAST2 have nearly the same finishing time of the reionization. Compared with the two late models, the difference of the ionization fraction evolution and the x_i - δT_b relation in the two early models are smaller. This can help us to discriminate the different reionization scenarios even if they have similar ionization fractions.

In real observations, the observed δT_b includes both signal and noise. To study the effect of the thermal noise on the 2d genus, we add a Gaussian noise to the signal map. We generated 500 maps with the random noise following the Gaussian distribution, where the standard deviation is $f\sigma_T$. where f is a constant, and

$$\sigma_T = \sqrt{\frac{\delta T_b - \langle \delta T_b \rangle}{N_c^2 - 1}}.$$

4. RESULTS

The observed signal can be characterized as the real signal convolved with the telescope response function or beam, however, the real telescope beam is complicated. To model the observed signal, in this paper we assume either a Gaussian or compensated Gaussian lobe function for simplicity. The Gaussian beam is simple, and widely used in the radio studies (e.g. Mao 2014; Wolz et al. 2014) to model the actual beam, which can be written as

$$F_G(\theta) = \frac{1}{2\pi\sigma^2} \exp\left(-\frac{\theta^2}{2\sigma^2}\right). \quad (9)$$

The full width at half maximum (FWHM) for the Gaussian beam is $\Delta\theta = 2\sigma\sqrt{2\ln 2}$. Another popular choice is

the compensated Gaussian,

$$F_{CG}(\theta) = \frac{1}{2\pi\sigma^2} \left(1 - \frac{\theta^2}{2\sigma^2}\right) \exp\left(1 - \frac{\theta^2}{2\sigma^2}\right). \quad (10)$$

The compensated Gaussian function approximates well the observational beam shape of a compact interferometer array (often referred to as ‘dirty beam’), which is insensitive to large-scale features. Eq. (10) shows that $F_G < 0$ if $\theta > \sqrt{2}\sigma$, i.e. the sign of the contribution is negative.

In Fig.2 we show the evolution of 21cm maps at the early, middle and late stage of reionization for the four models: (a) HRT sim1, (b) HRT sim2, (c) 21cmFAST1, (d) 21cmFAST2. In each of the subfigures, the top panels represent the original δT_b signal, the middle and bottom panels are the simulated observed map with the Gaussian and compensated Gaussian beam profile, respectively. We can see that there even though both the HRT sim1 and 21cmFAST1 models have relatively late reionization, there are significant differences between the two models at each epoch. In the HRT sim1, the ionized regions are diffused, while it is linked together in 21cmFAST1. Similarly, for the two early reionization models (HRT sim2 and 21cmFAST2), there are also distinctive differences. This indicates that the reionization process in the HRT simulation and that in the 21cmFAST are different. For the two 21cmFAST simulations, the distributions of δT_b are similar if they have the same ionization fraction x_i . Since the Gaussian and compensated Gaussian beam can smooth the δT_b distribution, the largest value of the δT_b decreases after the smoothing. As explained above, the compensated Gaussian beam can produce negative values, therefore, δT_b is negative in some regions with the compensated Gaussian beam.

In order to compare the topology results with those from the power spectrum, we also calculate the angular power spectrum $[l(l+1)C_l/2\pi]^{1/2}$. In Figure 3 we plot the angular power spectrum of δT_b for the four models with different redshifts. It is seen that the shape of the angular power spectrum is nearly the same for the early and middle phase of reionization in the four simulations. Except for HRT sim1, the shape of the angular power spectra in the late phase of reionization are also similar, hence it would be difficult to distinguish the different reionization scenarios from the angular power spectrum, while the topology offers a way to distinguish them.

In Figure 4, we show the 2d genus for both the differential brightness temperature (solid lines) and the gas (or matter) density (dashed lines) in the four simulations. On the scale discussed here, the gas (or matter) density distribution is nearly Gaussian, so from the comparison between the density and δT_b genus curve, we can see how far do the 21cm signal deviates from Gaussian. In each figure, the left and right panels show the results from the Gaussian beam and compensated Gaussian beam, respectively. Since Panel (a) and (b) belong to the same kind of simulation, and Panel (c) and (d) belong to the same kind of simulation, and the ionization fraction are also similar, the genus curve on the left and right panels look similar.

It is noted that the 2d genus curve from the Gaussian beam is virtually indistinguishable from the compensated Gaussian one. The compensated Gaussian beam has a Gaussian-type peak in the middle, surrounded by

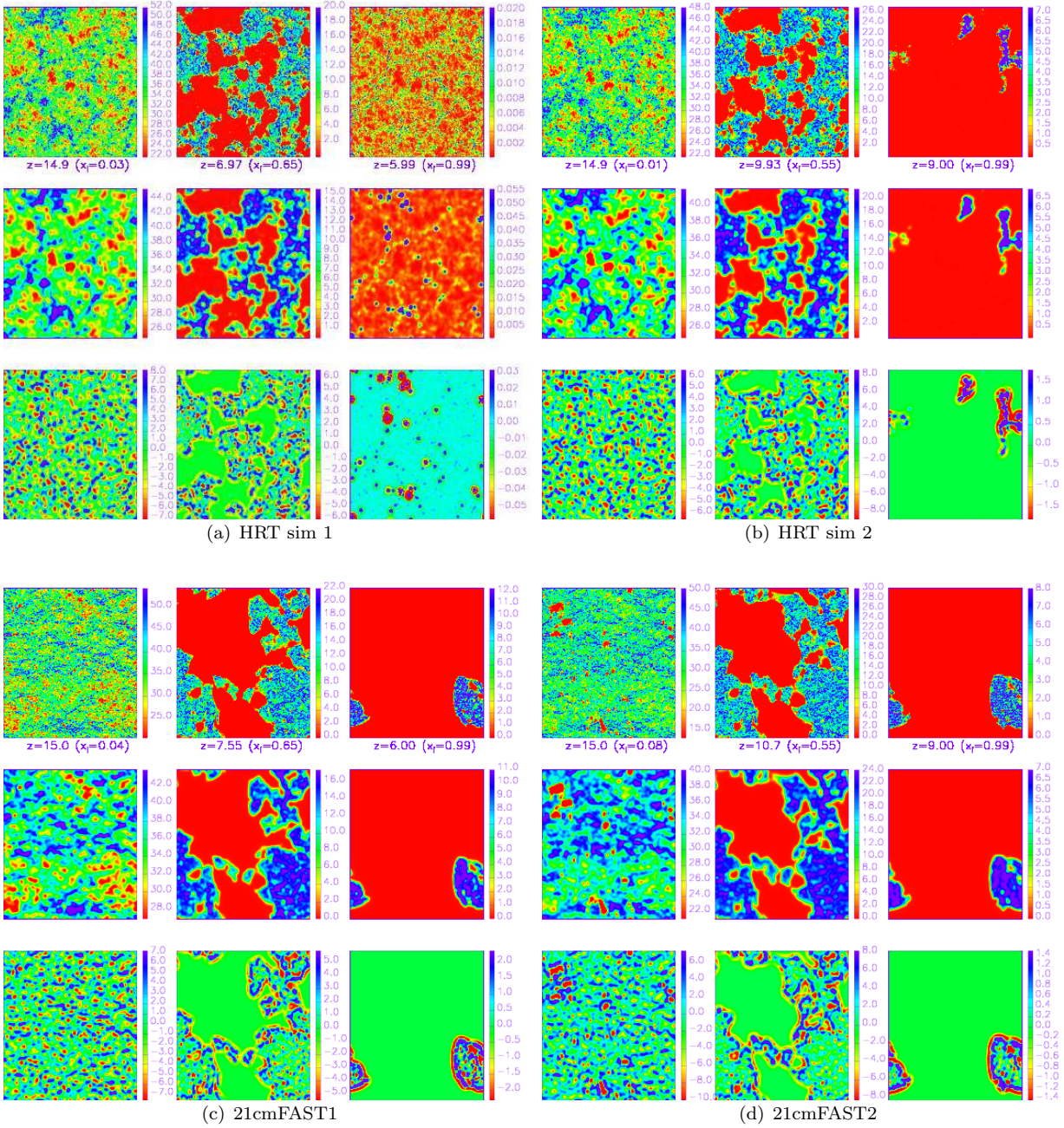


FIG. 2.— The 21cm maps for the four models: (a) HRT sim1, (b) HRT sim2, (c) 21cmFAST1, (d) 21cmFAST2. For each model, three redshifts are plotted (marked on the figure). Also, for each model, the Top panel shows the original δT_b map with frequency bin width $\Delta\nu = 0.2$ MHz. The high and low differential brightness temperature regions are the neutral and ionized ones respectively. The unit of the color bar is mK. The Middle and bottom panels show the simulated "observed map" with the Gaussian and compensated Gaussian beams respectively, with beam width $\Delta\theta = 1'$.

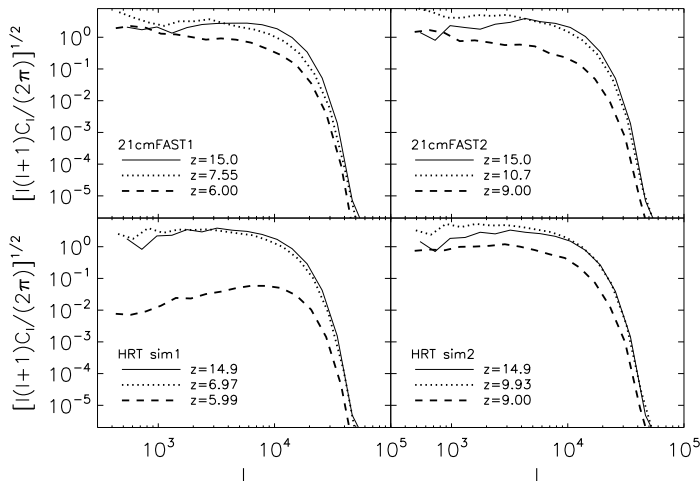


FIG. 3.— 2d angular power spectrum of δT_b for four models with different redshifts.

a negative wing, which adds small wiggles to the real signals. Therefore, the compensate Gaussian beam change the topology of the differential brightness temperature slightly (Hong et al. 2014). More detailed comparison of these two beams are shown in Hong et al. (2014). In this paper we only present the results for the two beam profiles here, and from now on we will only discuss the results obtained with the Gaussian beam.

For each model, the 2d genus curve of the differential brightness temperature is distinctly different at different ionization fractions or redshifts. Furthermore, even at the same ionization fraction, the 2d genus curves for different reionization models are significantly different. This can be seen clearly from the middle panels in Fig. 4. Quantitatively, we can make a Kolmogorov-Smirnov (KS) test, which is used to test whether two distributions are different. Usually, the KS-test gives the deviation between two probability distribution functions of a single independent variable, but it is also valid to distinguish two any arbitrary distributions, that is, the multivariate distribution. Here we take $G(\nu)$ as the distribution function of the threshold ν , and apply the KS-test to the $G(\nu)$ functions. Note that we are not testing the distribution of the 21 cm brightness temperature, but comparing the shape of the genus curves $G(\nu)$, taking it as if it the distribution of the single variable ν . The significance level of an observed value of D , which is a disproof of the null hypothesis that the distributions are the same, is given by (Press et al. 1992) :

$$\text{prob}(D > \text{observed}) = Q_{KS} \left(\left[\frac{\sqrt{N_e} + 0.12 + 0.11/\sqrt{N_e}}{\sqrt{N_e}} \right] D \right) \quad (11)$$

where D is defined as the maximum value of the absolute difference between two cumulative distribution functions, $N_e = \frac{N_1 N_2}{N_1 + N_2}$ (N_1 and N_2 are the data number in distribution 1 and 2, respectively), and the function Q_{KS} is defined as

$$Q_{KS}(\lambda) = 2 \sum_{j=1}^{\infty} (-1)^{j-1} \exp(-2j^2 \lambda^2) \quad (12)$$

Small values of prob imply that the distribution 1 is significantly different from that of distribution 2. We refer

the interested reader to the book (Press et al. 1992) for the detail description of the KS test. The result shows that the genus curve from HRT sim1 at $x_i = 0.65$ is different from that from 21cmFAST1 at $x_i = 0.65$ with confidence level higher than 97%.

In the early phase of reionization, i.e. $x_i \leq 0.08$, the universe is nearly neutral, the differential brightness temperature of HI, δT_b , still follows the Gaussian distribution, which can be seen from the bottom left panels in the subfigures of Fig. 4. The amplitude of the δT_b genus curve is larger than the gas density genus curve at $\nu \sim -1$ at $z = 14.9$ in HRT sim1. The major reason for this is that the star formation is already occurring during this epoch, and some regions have already been ionized, which increase the number of low-density regions. In simulations 21cmFAST1 and 21cmFAST2, the 2d genus curve of δT_b is distinguishable from the matter curve: the amplitude of the 2d genus curve of δT_b is larger than that of the matter from low ν to high ν . This is the result of a combination of two reasons. First, similar to the HRT sim1 and HRT sim2 models, the universe has begun to ionize at this redshift, both new islands of HI regions and the lake of HII regions have formed, the former corresponds to the isolated high-density regions, while the later is responsible for the low-density regions, the same findings were also presented in Hong et al. (2014). Second, the value of δT_b is related to the comoving velocity gradient of gas along the LOS dv_r/dr , see Eq. (4). We find that dv_r/dr in simulation HRT sim1 and HRT sim2 is tiny, while those in simulation 21cmFAST1 and 21cmFAST2 are relatively large.

In the middle phase of reionization, i.e., $0.55 \leq x_i \leq 0.65$, many bubbles exist and some of them overlap, therefore, the amplitude of genus curve of δT_b is nearly zero at low ν and the genus curve of δT_b is shifted to the right compared with the genus curve of the gas (or matter). This shift is consistent with the result in Figure 2 of Kim & Park (2007). In their studies, the genus curve for a uniform disk with randomly distributed empty holes shifts to the right. The amplitude of the 2d genus curve of δT_b in the high ν still keeps the vestiges of its initial curve. This is because the high-density regions are still shielded from the ionized photons to ionize the rest of the universe (Lee et al. 2008).

In the late epoch of reionization, i.e., $x_i \leq 0.99$, the universe is almost completely ionized, the genus of δT_b from HRT sim1 shows that the remaining HI nearly follows the matter distribution, which agrees with the result given in Lee et al. (2008). Although $x_i = 0.99$ at redshift $z = 8.9954$ in HRT sim2, there are still some neutral patches, and the amplitude of the genus curve for δT_b is higher than that of the matter distribution. For the two 21cmFAST simulations, the ionized bubble has merged except for very low density regions, therefore, the genus curves of δT_b at low ν is nearly zero.

In Figure 5, we show the effect of the thermal noise on the genus curve. It is seen that the genus curve is not affected in the early phase of reionization. The reason is that the brightness temperature δT_b follows the Gaussian distribution, when an additional Gaussian noise is included, the distribution of δT_b is still Gaussian. In the middle and late epoch of reionization, the effect of the thermal noise on the genus curve is significant. The amplitude of the genus curves with thermal noise are larger

than those without thermal noise due to merging of bubble. This effect is in some sense similar to what was shown in Fig.5 of Melott et al. (1989), where the amplitude of the genus curve is decreased after structure formation. Nevertheless, as demonstrated by the KS test, the two ionized models can still be distinguished clearly even when $1\sigma_T$ noise is added.

In Figure 6, the PDF of the 2d genus $G(\nu)$ at $\nu=-2, -1, 0, 1, 2$. are plotted for the HRT sim1 model at $z = 5.99$ with 1σ thermal noise added. These PDFs of the 2d genus show that they are centered at certain value, with nearly Gaussian distribution. Thus, in making model test it is reasonable to assume Gaussian likelihood for the genus measurement.

In Figure 7, we compare the 2d angular power spectrum (left panels) and the 2d genus curve (right panels) for the four different reionization models at the same redshift $z = 9.00$ with and without 1σ thermal noise. We can also obtain some statistical confidence level from these tests—the different models can be compared using the KS test with the angular power spectrum data and the 2d genus curves (See Table 1). Here we take the angular power spectrum as the distribution function of the single variable l . From the value of *prob*, we know that the 21cmFAST1 model can be better distinguished with the other three models by using the 2d angular power spectrum, while the 21cmFAST2 model can be better distinguished by using the 2d genus curve if there is no thermal noise.

The Gaussian thermal noise does not affect the angular power spectrum, but it can reduce the non-Gaussian signal of the 2d genus. From the lower part of Table 1, we see that the HRT sim2 model can not be distinguished from the 21cmFAST2 model by using either the power spectrum or genus method from the KS test if 1σ thermal noise is included. We also use the χ^2 test and probability to exceed (PTE) to distinguish different models using the 21 cm power spectrum and the 2d genus curve. The χ^2 test is defined as

$$\chi^2 = \sum_{i=1}^{N_{\text{bin}}} \frac{(y_{i,1} - y_{i,2})^2}{|y_{i,2}|} \quad (13)$$

where $y_{i,1}$ and $y_{i,2}$ are the distribution in i th bin for model 1 and 2, respectively. N_{bin} is the number of bins and $N_{\text{bin}} = 31$ for the 2d genus curve and $N_{\text{bin}} = 20$ for the angular power spectrum. Given an input χ^2 and the number of degrees of freedom ν' , the PTE can be calculated by

$$PTE = \frac{1}{2^{\nu'/2}\Gamma(\nu'/2)} \int_{\chi^2}^{\infty} t^{\nu'/2-1} e^{-t/2} dt \quad (14)$$

A small value of PTE indicates that two models are different. In Table 1, we also give the values of χ^2/ν' and PTE for both the power spectrum and genus without and with 1σ noise. Here, we assume that there are two different parameters when we use the χ^2 /PTE test to compare each pair of these simulations. Obviously, the χ^2 /PTE tests tell us that the 2d genus curves from different reionized models can be easily distinguished even 1σ thermal noise is added. However, it is difficult to distinguish models HRT sim1 with HRT sim2, HRT sim1

with 21cmFAST2, and HRT2 with 21cmFAST2 from the angular power spectrum method. It seems that the results from the χ^2 /PTE test are inconsistent with those from the KS test for some comparisons, such as HRT sim2 to 21cmFAST2 by using the 2d genus curves with 1σ thermal noise. The reason is that the value of *prob* from KS test depends on the deviation between two cumulative distribution function, one discrete data in each bin can not affect the *prob* significantly, while the value of χ^2 can be very large even the difference of two models in one bin is significant. Combined with the KS test and χ^2 /PTE test for the signals with and without 1σ noise, we know that the 2d genus and angular power spectrum are complementary. Moreover, the shape of the power spectrum are nearly the same for the different reionization models, and the only difference is the amplitude, however, it is difficult to obtain the accurate amplitude of the power spectrum in observations. From this perspective the genus method has its niche when compared with the widely used power spectrum.

5. SUMMARY AND DISCUSSION

We quantify the 2d topology of the 21cm differential brightness temperature field for two HRT simulations and two semi-analytical models. It is shown that the 2d topology of δT_b is significantly different for different reionization models even $1\sigma_T$ thermal noise is added. For the same simulation, the 2d topology at different redshifts reflects the status of reionization.

We show the results for both Gaussian and compensated Gaussian beam filter of the telescopes. It is shown that the brightness temperature maps filtered with these beam patterns can be used to discriminate different reionization scenarios through the study of the 2d genus topology. However, the beam filter is more complicated in practice, and we need to consider the special case for different telescope. Moreover, the foreground removing is crucial for the detection of the neutral HI signals, which is beyond our study in the current paper. Of course, this is our first step by using the 2d topology of the 21 cm differential brightness to constrain cosmic reionization. The 2d topology can become a very powerful tool for probing the reionization history and hope that the real two dimension topology of neutral hydrogen at high redshift can be observed by the future telescopes like SKA.

ACKNOWLEDGMENTS

We thank the referee for comments and suggestions that improved the paper. This work has started during YGW's visit to KIAS 2012, and he would like to express his gratitude for KIAS. We thank Hy Trac and Renyue Cen for providing us the HRT simulation data. We also thank Xin Wang and Bin Yue for many helpful discussions. This work is supported by the Ministry of Science and Technology 863 project grant 2012AA121701. YGW acknowledges the 973 Program 2014CB845700, and the NSFC grant 11390372. YDX is supported by NSFC grant No. 11303034. XLC acknowledges the support of the 973 program (No.2007CB815401,2010CB833004), the CAS Knowledge Innovation Program (Grant No. KJCX3-SYW-N2), and the NSFC grant 10503010. XLC is also supported by the NSFC Distinguished Young Scholar Grant No.10525314.

TABLE 1
prob VALUES FROM KS TEST AND χ^2/ν' (*PTE*) FROM χ^2/PTE TEST FOR DIFFERENT REIONIZATION MODELS AT $z = 9$ WITH AND WITHOUT 1σ THERMAL NOISE.

	<i>prob</i> (power spectrum)	<i>prob</i> (genus)	χ^2/ν' (<i>PTE</i>) (power spectrum)	χ^2/ν' (<i>PTE</i>) (genus)
HRT sim1: HRT sim2	0.13	0.36	0.36(0.99)	33.98 (0)
HRT sim1: 21cmFAST1	8.16E-3	0.36	5.73(0)	42.22 (0)
HRT sim1: 21cmFAST2	0.28	8.08E-4	0.89(0.60)	89.12 (0)
HRT sim2: 21cmFAST1	2.57E-3	0.78	6.48(0)	77.83 (0)
HRT sim2: 21cmFAST2	0.77	5.65E-3	0.18(1.00)	75.48 (0)
21cmFAST1:21cmFAST2	2.57E-3	2.21E-3	1.50 (0.08)	35.39 (0)
HRT sim1: HRT sim2 (+1 σ)	0.13	0.36	0.36(0.99)	137.22(0)
HRT sim1: 21cmFAST1 (+1 σ)	8.16E-3	0.36	5.78(0)	42.98(0)
HRT sim1: 21cmFAST2 (+1 σ)	0.28	0.36	0.89(0.60)	184.34(0)
HRT sim2: 21cmFAST1 (+1 σ)	2.57E-3	6.21E-2	6.42(0)	321.39(0)
HRT sim2: 21cmFAST2 (+1 σ)	0.77	0.99	0.18(1.00)	18.03(0)
21cmFAST1:21cmFAST2 (+1 σ)	2.57E-3	6.21E-2	1.50(0.08)	1168(0)

REFERENCES

- Barkana, R. & Loeb, A. 2001, *Phys. Rep.*, 349, 125
 Battaglia, N., Trac, H., Cen, R., & Loeb, A. 2013, *ApJ*, 776, 81
 Bowman, J. D., Cairns, I., Kaplan, D. L., et al. 2013, *PASA*, 30, 31
 Cen, R., McDonald, P., Trac, H., & Loeb, A. 2009, *ApJ*, 706, L164
 Chepurnov, A., Gordon, J., Lazarian, A., & Stanimirovic, S. 2008, *ApJ*, 688, 1021
 Choi, Y.-Y., Park, C., Kim, J., et al. 2010, *ApJS*, 190, 181
 Choudhury, T. R. & Ferrara, A. 2007, *MNRAS*, 380, L6
 Coles, P. 1988, *MNRAS*, 234, 509
 Colley, W. N., Gott, III, J. R., & Park, C. 1996, *MNRAS*, 281, L82
 Dunkley, J., Komatsu, E., Nolta, M. R., et al. 2009, *ApJS*, 180, 306
 Fan, X., Carilli, C. L., & Keating, B. 2006, *ARA&A*, 44, 415
 Furlanetto, S. R., Oh, S. P., & Briggs, F. H. 2006, *Phys. Rep.*, 433, 181
 Furlanetto, S. R., Zaldarriaga, M., & Hernquist, L. 2004, *ApJ*, 613, 1
 George, E. M., Reichardt, C. L., Aird, K. A., et al. 2015, *ApJ*, 799, 177
 Gott, J. R., Choi, Y., Park, C., & Kim, J. 2009, *ApJ*, 695, L45
 Gott, III, J. R., Dickinson, M., & Melott, A. L. 1986, *ApJ*, 306, 341
 Gott, III, J. R., Park, C., Juskiewicz, R., et al. 1990, *ApJ*, 352, 1
 Gott, J. R. I., Hambrick, D. C., Vogeley, M. S., et al. 2008, *ApJ*, 675, 16
 Gott, J. R. I., Miller, J., Thuan, T. X., et al. 1989, *ApJ*, 340, 625
 Gott, J. R. I., Weinberg, D. H., & Melott, A. L. 1987, *ApJ*, 319, 1
 Hamilton, A. J. S., Gott, J. R. I., & Weinberg, D. 1986, *ApJ*, 309, 1
 Hong, S. E., Ahn, K., Park, C., et al. 2014, *Journal of Korean Astronomical Society*, 47, 49
 Iliev, I. T., Mellema, G., Ahn, K., et al. 2014, *MNRAS*, 439, 725
 Iliev, I. T., Mellema, G., Pen, U.-L., et al. 2006, *MNRAS*, 369, 1625
 Jacobs, D. C., Pober, J. C., Parsons, A. R., et al. 2015, *ApJ*, 801, 51
 James, J. B., Lewis, G. F., & Colless, M. 2007, *MNRAS*, 375, 128
 Kim, H.-S., Wyithe, J. S. B., Raskutti, S., Lacey, C. G., & Helly, J. C. 2013, *MNRAS*, 428, 2467
 Kim, S. & Park, C. 2007, *ApJ*, 663, 244
 Lee, K.-G., Cen, R., Gott, III, J. R., & Trac, H. 2008, *ApJ*, 675, 8
 Lewis, A. & Challinor, A. 2007, *Phys. Rev. D*, 76, 083005
 Liu, A. & Tegmark, M. 2011, *Phys. Rev. D*, 83, 103006
 Majumdar, S., Mellema, G., Datta, K. K., et al. 2014, *MNRAS*, 443, 2843
 Mao, X.-C. 2014, *ApJ*, 790, 148
 Mao, Y., Shapiro, P. R., Mellema, G., et al. 2012, *MNRAS*, 422, 926
 Matsubara, T. & Jain, B. 2001, *ApJ*, 552, L89
 Mellema, G., Iliev, I. T., Alvarez, M. A., & Shapiro, P. R. 2006, *NewA*, 11, 374
 Melott, A. L., Cohen, A. P., Hamilton, A. J. S., Gott, III, J. R., & Weinberg, D. H. 1989, *ApJ*, 345, 618
 Mesinger, A. & Furlanetto, S. 2007, *ApJ*, 669, 663
 Mesinger, A., Furlanetto, S., & Cen, R. 2011, *MNRAS*, 411, 955
 Mesinger, A., McQuinn, M., & Spergel, D. N. 2012, *MNRAS*, 422, 1403
 Mortonson, M. J. & Hu, W. 2010, *Phys. Rev. D*, 81, 067302
 Paciga, G., Albert, J. G., Bandura, K., et al. 2013, *MNRAS*, 433, 639
 Park, C., Choi, Y., Vogeley, M. S., et al. 2005a, *ApJ*, 633, 11
 Park, C., Colley, W. N., Gott, III, J. R., et al. 1998, *ApJ*, 506, 473
 Park, C. & Gott, III, J. R. 1991, *ApJ*, 378, 457
 Park, C., Gott, III, J. R., & Choi, Y. J. 2001, *ApJ*, 553, 33
 Park, C., Gott, III, J. R., Melott, A. L., & Karachentsev, I. D. 1992, *ApJ*, 387, 1
 Park, C., Kim, J., & Gott, J. R. I. 2005b, *ApJ*, 633, 1
 Park, C. & Kim, Y.-R. 2010, *ApJ*, 715, L185
 Park, C., Pranav, P., Chingambam, P., et al. 2013, *Journal of Korean Astronomical Society*, 46, 125
 Park, C.-G. 2004, *MNRAS*, 349, 313
 Planck Collaboration, Ade, P. A. R., Aghanim, N., et al. 2015, *ArXiv e-prints*
 Press, W. H., Teukolsky, S. A., Vetterling, W. T., & Flannery, B. P. 1992, *Numerical recipes in FORTRAN. The art of scientific computing*
 Rottgering, H. J. A., Braun, R., Barthel, P. D., et al. 2006, *ArXiv Astrophysics e-prints*
 Sato, J., Umetsu, K., Futamase, T., & Yamada, T. 2003, *ApJ*, 582, L67
 Sunyaev, R. A. & Zeldovich, I. B. 1980, *MNRAS*, 190, 413
 Sunyaev, R. A. & Zeldovich, Y. B. 1972, *Comments on Astrophysics and Space Physics*, 4, 173
 Tingay, S. J., Goeke, R., Bowman, J. D., et al. 2013, *PASA*, 30, 7
 Trac, H. & Cen, R. 2007, *ApJ*, 671, 1
 Trac, H., Cen, R., & Loeb, A. 2008, *ApJ*, 689, L81
 Vogeley, M. S., Park, C., Geller, M. J., Huchra, J. P., & Gott, J. R. I. 1994, *ApJ*, 420, 525
 Wang, X., Chen, X., & Park, C. 2012, *ApJ*, 747, 48
 Wolz, L., Abdalla, F. B., Blake, C., et al. 2014, *MNRAS*, 441, 3271
 Wu, X. 2009, in *Bulletin of the American Astronomical Society*, Vol. 41, American Astronomical Society Meeting Abstracts, 226.05
 Xu, Y., Chen, X., Fan, Z., Trac, H., & Cen, R. 2009, *ApJ*, 704, 1396
 Yue, B. & Chen, X. 2012, *ApJ*, 747, 127
 Yue, B., Ciardi, B., Scannapieco, E., & Chen, X. 2009, *MNRAS*, 398, 2122
 Zahn, O., Reichardt, C. L., Shaw, L., et al. 2012, *ApJ*, 756, 65
 Zhang, J., Hui, L., & Haiman, Z. 2007, *MNRAS*, 375, 324

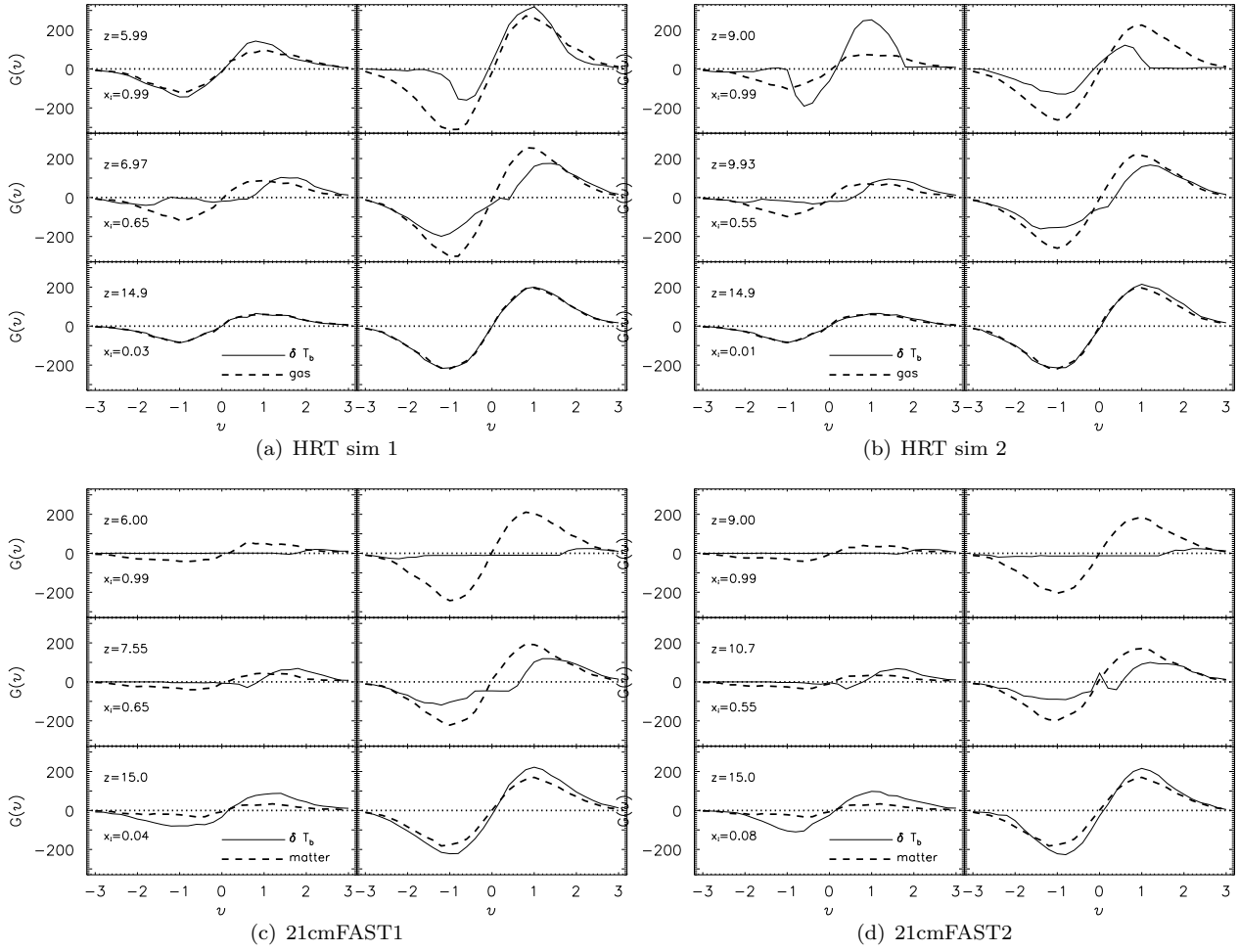


FIG. 4.— The 2d genus of δT_b (solid) and gas distribution (dashed) at different redshifts for (a) HRT sim1, (b) HRT sim2, (c) 21cmFAST1, (d) 21cmFAST2 models. In each model, the left panels show the results for Gaussian beam while the right ones represent results for compensated Gaussian filter.

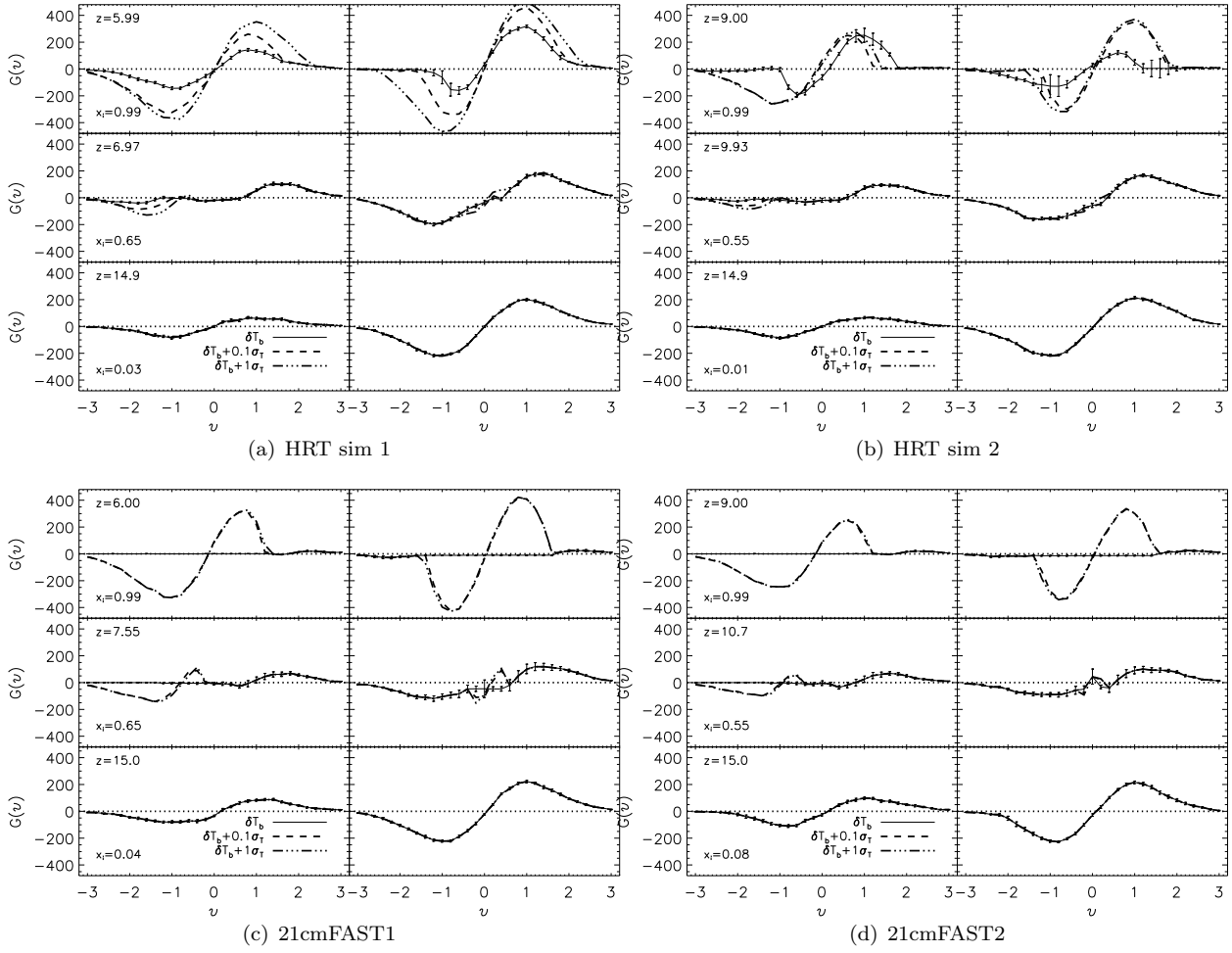


FIG. 5.— Similar to Figure 4, but with Gaussian noise added. In each panel, the solid line represent the genus curve without the thermal noise, while the dashed and dash-dot lines represents the results with $0.1\sigma_T$ and σ_T thermal noise added, respectively. The error bar in the solid line is estimated by 30 similar simulated data samples.

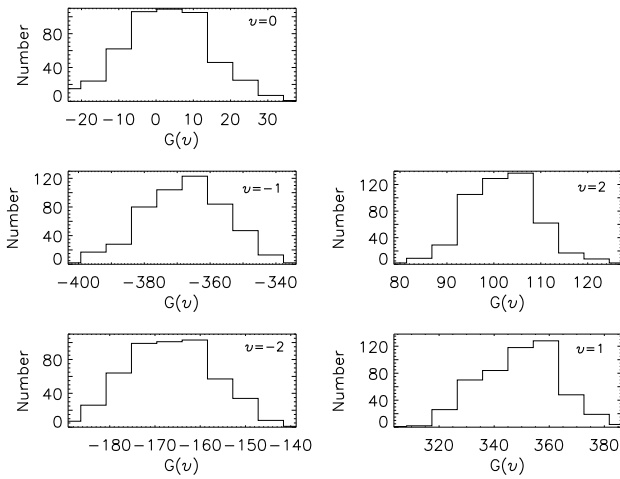


FIG. 6.— Probability density function of the 2d genus including $1\sigma_T$ Gaussian noise for HRT sim1 at $z = 5.99$ for $\nu = -2, -1, 0, 1, 2$.

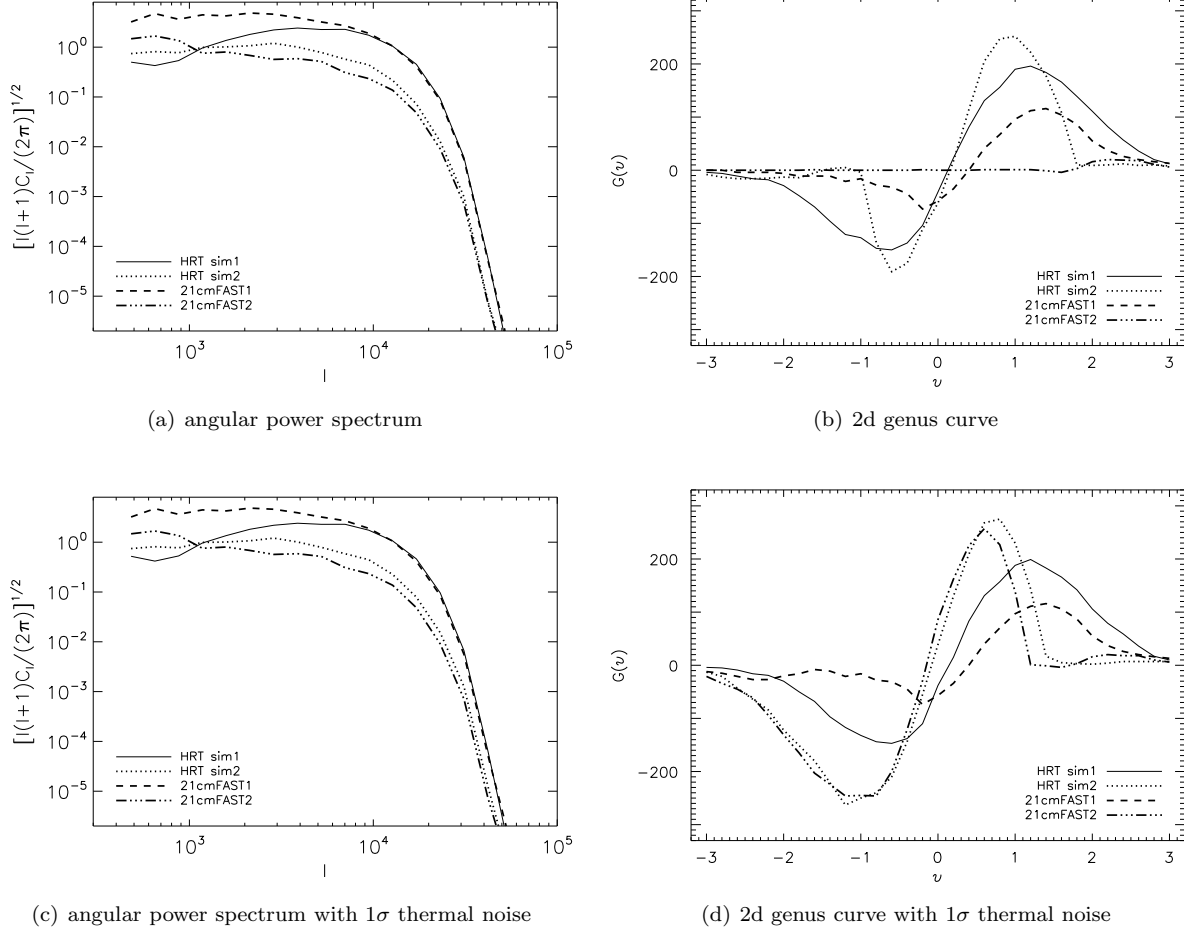


FIG. 7.— (a) 2d angular power spectrum of δT_b for four models with the same redshift $z = 9.00$. (b) 2d genus distribution of δT_b for four models with the Gaussian beam with the same redshift $z = 9.00$. (c) similar to (a), but for the results with 1σ thermal noise. (d) similar to (c), but for the results with 1σ thermal noise.